A NOVEL APPROACH TO AUTOMATED TRACKING CONTROL OF HYBRID TILTING ROTOR UAVS USING LQG CONTROLLER AND STATE MACHINE

Joshua Levin Kurniawan[1], Patrisius Bagus Alvito Baylon[1] & Rianto Adhy Sasongko[1]

[1] Faculty of Mechanical and Aerospace Engineering, Institut Teknologi Bandung, Jl.E ITB, Kota Bandung, Jawa Barat 40132, Indonesia

Abstract

Tilt-rotor UAVs offer several benefits, primarily their ability to perform vertical takeoff and vertical landing while being capable of forward flight in fixed-wing mode. However, implementing control for this type of UAV can be challenging, especially during the transition phase, where the system characteristics can change significantly and may introduce nonlinearities. Current methodologies typically rely on linearizing the dynamics at several trim points, which is unsuitable due to the finite number of linearization points, resulting in inadequate consideration of aerodynamic effects. This paper introduces a novel approach to designing a tracking controller for tilt-rotors by employing an a set of linear-quadratic-gaussian controllers coupled with a state-machine. The operation of the tilt-rotor UAV is decomposed into several operating points, which are then linearized. Based on the linearization results, a set of linear-quadratic controllers and Kalman Filters are designed. These controllers and observers are activated using a switching algorithm controlled by the state machine. The conducted simulation, the tilt-rotor UAV demonstrates that the designed controller is notably capable of maintaining stable hover, transition, and fixed-wing operations autonomously. The test results show that the designed control system can execute a stable transition phase within 32 seconds, with a total displacement of 289.3 m horizontally and 50.6 m vertically. Remarkably, the proposed method also achieves accurate tracking capability, with errors of 0.425% and 0.105% for hover and fixed-wing operations, respectively.

Keywords: tilt-rotor, transition, LQG, state machine

1. Introduction

One advantage of the tilt-rotor UAV configuration is its ability to exploit the efficiency of fixed wing configuration and the flexibility of rotorcraft configuration during its flight. This dual capability offers flexibility in mission planning and execution, as the UAV can efficiently cover large areas in fixed-wing mode while also conducting precise maneuvers and tasks in rotorcraft mode. Additionally, the ability to transition seamlessly between these modes enhances the UAV's adaptability to different operational environments and tasks, making it suitable for a wide range of applications, from aerial mapping and surveillance to search and rescue missions [1].

One important phase in the operation of UAVs equipped with tilt-rotor configuration is the transition phase from fixed-wing flight to hover, which is usually performed autonomously. Therefore, an automatic control system is required to perform this transition phase. However, designing an automatic control system during the transition phase presents its own challenges. In this phase, the dynamics of the tilt-rotor are complex and nonlinear, so a standard implementation of linear time-invariant control system cannot be applied.

The challenges associated with nonlinearities in transitions are commonly addressed by linearizing the model around various trim points within the feasible flight envelope. For each of these points, a linear control law is designed. In previous research, a combination of these linear control laws with Gain Scheduling is employed. Gain scheduling technique involves adapting the controller gains of

a dynamic system based on changing operating parameters to achieve continuous control across the entire flight envelope. Previous study has shown the combination of linear control laws, such as proportional-integral-derivative (PID) with gain scheduling [2], state feedback with gain scheduling[3], and linear-quadratic-controller with gain scheduling[4]. However, using this approach of linearized model, aerodynamic effects acting on the vehicle during transition can often not be considered adequately, meaning that stable and feasible trajectory generation is not guaranteed, due to a finite number of linearization points [5].

Another approach to controlling the transition phase is by using model predictive control (MPC). Previous research that has been validated through experiments shows that using this approach, a successful automatic transition from rotary-wing to fixed-wing flight mode and back was achieved in the presence of wind disturbances, demonstrating the MPC's capability to ensure sufficient lift generation despite the changing aerodynamic effects [5]. However, real-time implementation of MPC is practically challenging due to the need for solving a constrained and potentially non-convex optimal control problem at each sampling instant [6]. The computation time may exceed the available time for control updates, impacting the system's responsiveness, especially when the computation is performed using the limited computational power provided by the onboard computer

To address the challenge of control, we develop a novel approach for the transition phase in a tilt-rotor UAV using a set of linear-quadratic-Gaussian (LQG) controllers and a state machine. The LQG controller is a control system that merges two approaches: the linear-quadratic controller and the Kalman filter. LQG as an optimal controllers are designed to minimize a specific cost function, offering better performance compared to some classical linear controllers, such as PID. With the incorporation of an appropriate Kalman Filter model, we can estimate the state of the aircraft even in the presence of Gaussian white noise and measurement errors[7]. This addition provides redundancy to ensure greater safety in the operation in the case of measurement errors during the transition phase. However, since the LQG model is built based on a linearized model, it would only be suitable for small disturbances and deviations, such that errors due to linear approximation are still acceptable. Therefore, for the transition case, we will apply linearization at several operating points and apply the LQG controller for each point.

This research will introduce a controller design that involved a state machine as a decision logic algorithm to select the suitable LQG algorithm for a certain state of the aircraft. A state machine is a mathematical abstraction used to design an algorithm that considers not only the algorithm's inputs but also the current state of the system to determine the appropriate output. In addition, a filter will be added to the system to smoothen the transient response between the state-switching. Utilizing a state machine, the optimization of the controller undergoes an offline process. This approach enables pre-computed optimizations, allowing the controller to anticipate and respond optimally to various operational scenarios in the transition phases without the need for continuous, resource-intensive onboard calculations. By making the computer work less during real control tasks, the suggested method ensures that the control system works better and responds faster to handle the vehicle's movements during transitions.

The proposed controller design framework will begin with constructing the nonlinear equations of motion for the UAV dynamics. By employing numerical methods, we will generate the Jacobian matrix of the system under various trim conditions, which will serve as the linearized equations of motion for the UAV. These linearized equations will then be utilized to design a set of linear quadratic Gaussian controllers.

2. Tilt-Rotor Dynamic System

2.1 Equation of Motions

In the tilt-rotor configuration, the UAV is equipped with two main rotors located in the front that can be tilted at specified angles and a fixed rear motor that is oriented downward. The two front rotors can be tilted at such an angle that when the two front motors tilt 90 degrees relative to the drone's longitudinal axis, both front motors, along with the rear motor, produce thrust upwards to allow the UAV to hover in rotorcraft mode. Meanwhile, when the two front motors align with the UAV's longitudinal axis, the drone will fly in fixed-wing mode. The RayBe UAV is also equipped with a V-Tail as the stabilizer.

The UAV has two different control surfaces, which are the ailerons used for roll maneuvers and the ruddervators used for pitch and yaw maneuvers. This configuration affects the equations of forces and moments acting on the aircraft. In hovering mode, the vertical thrust produced by all three motors counteracts the gravitational force, and the control of the UAV involves balancing the moments to maintain stability. In fixed-wing mode, the aerodynamic forces and moments become predominant, and the UAV behaves like a conventional aircraft, relying on aerodynamic lift, drag, and control surfaces to maneuver.

Our focus lies solely on studying the UAV's motions within the longitudinal plane, as the predominant motion during the transition phase occurs within this plane. The aircraft's longitudinal motion encompasses three degrees of freedom: two translations along the X and Z axes of the aircraft's body, and one rotational motion with the Y-body axis serving as the center of rotation, known as pitching. The aircraft is assumed to be in symmetric flight, which means there is no translational or angular acceleration occurring in the aircraft's lateral and directional axes. The equation of motion for the aircraft under steady flight conditions can be written in Equation 1 [8].

$$\begin{aligned} -W\sin\theta + X &= m(\dot{u} + qw), \\ W\cos\theta + Z &= m(\dot{w} - qu), \\ M &= I_y\dot{q}, \\ \dot{\theta} &= q \end{aligned} \tag{1}$$

In Equation 1, the variables are defined as follows: W represents the weight of the aircraft, θ, X, and Z denote the forces acting in the X and Y body axes respectively, M represents the moment occurring in the aircraft within the longitudinal plane, m stands for the mass of the aircraft, u and w indicate the velocity of the aircraft along the X and Z body axes, q represents the pitch rate of the aircraft, and I_y represents the aircraft's moment of inertia around Y-body axis.

In the tilting rotor configuration, two motors located at the front can be tilted at such an angle that when the two front motors tilt 90 degrees relative to the drone's longitudinal axis, both front motors, along with the rear motor, produce thrust upwards to allow the UAV to hover. Meanwhile, when the two front motors align with the UAV's longitudinal axis, the drone will fly in fixed-wing mode.

The forces and moments acting on the aircraft can be decomposed into several components. Primarily, aerodynamic forces, comprising lift denoted as L and drag denoted as D, contribute significantly. Secondly, propulsion forces generated by the front and rear rotors are labeled as T_{front} and T_{aft} respectively, with T_{front} representing the combined force from both front motors. Additionally, the aerodynamic moment is represented by M_{aero}. Figure 1 provides an illustration of the aircraft's forces and moments, alongside other parameters essential for mathematically characterizing the force and moment equations in the UAV's longitudinal plane. Here, δ_{tilt} signifies the tilt angle of the front motors, d_{r_x} denotes the X-body axis distance from the center of thrust of the rear motor to the center of gravity, d_{f_x} and d_{f_z} represent the horizontal and vertical distances of the front motors' center of thrust to the aircraft's center of gravity respectively, and δ_e denotes the deflection angle of the elevator. Thus, we can formulate equations describing the forces acting on the X and Z body axes of the aircraft, along with the moment in the aircraft's longitudinal plane, as detailed in Equation 2.

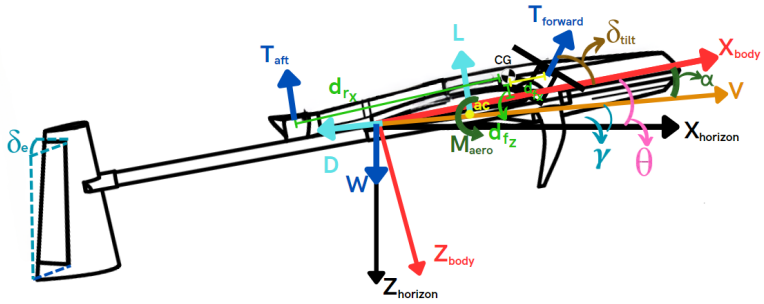

Figure 1 – Forces and moments diagram of tilt-rotor UAV in the longitudinal plane

$$\begin{aligned} X &= T_{front}\cos\delta_{tilt} - D\cos\alpha - L\sin\alpha, \\ Z &= T_{front}\sin\delta_{tilt} + T_{rear} - D\sin\alpha + L\cos\alpha, \\ M &= T_{front}\left(-\cos\delta_{tilt}d_{f_z} + \sin\delta_{tilt}d_{f_x}\right) - T_{rear}d_{r_x} + M_{aero} \end{aligned} \tag{2}$$

The lift, drag, and aerodynamic moment outlined in Equation 2 are influenced by various factors, including the aircraft's angle of attack α, the deflection of the elevator δ_e, and the pitching rate q. Equation 3 only applies to small deviations of α. Within this context, C_{L_0}, C_{D_0}, and C_{M_0} denote the non-dimensional free coefficients of the aircraft's lift, drag, and aerodynamic moment, respectively. Furthermore, C_{L_α}, C_{D_α}, and C_{M_α} represent the changes in the aircraft's aerodynamic lift, drag, and moment coefficients with respect to α. Additionally, C_{L_q} denotes the change in the lift coefficient with respect to the non-dimensionalized form of the aircraft's pitch rate $\tilde{q}$, as defined in Equation 4, where $\bar{c}$ is the mean aerodynamic chord of the aircraft. Finally, ρ, V, and S correspond to atmospheric air density, aircraft velocity, and wing area, respectively.

$$\begin{aligned} D &= \frac{1}{2}\rho V^2 S\left(C_{D_0} + C_{D_\alpha}\alpha + C_{D_{\delta_e}}\delta_e\right) \\ L &= \frac{1}{2}\rho V^2 S\left(C_{L_0} + C_{L_\alpha}\alpha + C_{L_q}q + C_{L_{\delta_e}}\delta_e\right) \\ M_{aero} &= \frac{1}{2}\rho V^2 S\bar{c}\left(C_{M_0} + C_{M_\alpha}\alpha + C_{M_{\delta_e}}\delta_e + C_{M_q}\tilde{q}\right) \end{aligned} \tag{3}$$

$$\tilde{q} = q\frac{\bar{c}}{2V} \tag{4}$$

The aerodynamic derivatives data in Equation 3 are obtained using XFLR 5 [9] and Digital Datcom software [10], for different variations of α and δ_e. As Equation 3 becomes unsuitable for approximating aerodynamic forces at large angles of attack, especially beyond the stall region, coefficients are approximated using a flat plate model to accurately model the aerodynamic force in these conditions [11]. An example of aerodynamic free coefficients and aerodynamic derivatives data for fixed-wing flight can be found in Table 1, which displays the parameter values for $\alpha = 0^\circ$. We conducted the analysis for $\alpha = -8.5^\circ$ to $\alpha = 12.5^\circ$ to obtain the parameter values for variations of α. The mass properties and geometrical parameter needed for Equation 1, 3, and 4 is given in Table 2.

Table 1 – Aerodynamic coefficient and aerodynamic derivative data

Lift coeficient		**Drag coeffiecient**		**Moment coefficient**	
C_{L_0}	0.252	C_{D_0}	0.016	C_{m_0}	-0.005
C_{L_α}	0.0886	C_{D_α}	0.00225	C_{m_α}	0.00143
$C_{L_{\delta_e}}$	0.00703	$C_{D_{\delta_e}}$	0.000824	$C_{m_{\delta_e}}$	-0.0128
C_{L_q}	0.0138	C_{D_q}	≈ 0	C_{m_q}	10.430

Table 2 – Aircraft Inertial Data and Geometrical Parameters

Parameter	**Value**
m	5.2 kg
I_y	0.0963 kg·m^2
S	0.428 m^2
b	1.838 m
$\bar{c}$	0.253 m

2.2 Trim Condition

To design the controller, we need to determine the trim condition of the aircraft, which is defined as the equilibrium state when the resultant force and moment are zero. We analyze this condition for fixed-wing flight, transition, and hover phases. Since our controller is specifically designed for the transition phase, it's crucial to assess trim conditions both before, during, and after this phase. This analysis examines the combination of T_{front}, T_{aft}, δ_e, u and w necessary to achieve the equilibrium condition.

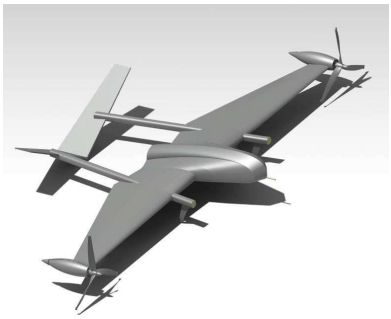

Figure 2 – Computer-aided design model of RayBe

In the transition controller modeling, we consider a case study of a RayBe UAV, shown in Figure 2, initially in hover flight with $u = 0$ m/s. Subsequently, the RayBe will perform a transition maneuver into fixed-wing forward flight until it achieves a velocity of 19 m/s, which is the typical cruise speed for RayBe UAV. We then divide the transition process into several trim conditions along the maneuver. For the hover phase, we divide the trim conditions into three different sets, each with varying vertical velocity. During the transition phase, we divide the trim conditions into five different conditions for the front motors: $\delta_{\text{tilt}} = 15°, 30°, 45°, 60°, 80°$. Finally, for the fixed-wing phase, we have two different trim conditions based on different aircraft velocities: 18 and $16 m/s$.
We applied several constraints to each phase of the trimmed flight. For the hover condition, the applied constraint is that there is no forward velocity of the tilt-rotor UAV. Therefore, $u = 0$ m/s. For the transition flight, we maintained the values of θ and q to become zero. For fixed-wing flight, the applied constraint is that the tilt-rotor UAV is flying in a steady straight flight. The mathematical definition for steady straight flight is described in Equation 5.

$$\dot{u} = \dot{v} = \dot{w} = 0, \quad \dot{p} = \dot{q} = \dot{r} = 0, \quad p = q = r = 0 \tag{5}$$

Additionally, we limited the value of elevator deflection δ_e to a range in which the minimum and maximum deflection values of the elevator are $-30°$ to $30°$. We then take examples of trimming under three different conditions: hover with a vertical velocity of 1 m/s, transition with $\delta_{tilt} = 60°$, and fixed-wing flight with $u = 18$ m/s. The trimming results are displayed in Table 3.

Table 3 – Trimming results of several example operating points

	Hover (w=1 m/s)	**Transition ($\delta_{\text{tilt}} = 60°$)**	**Fixed Wing (u =18 m/s)**
T_{front} **(N)**	35.2941	8.2244	0.046402
T_aft **(N)**	9.7187	0	0
δ_e **(rad)**	0.5236	0.5236	-0.0014791
u **(m/s)**	0	4	18
w **(m/s)**	-1	0	0.89443
θ **(rad)**	0	0	0.0057106
q **(rad/s)**	0	0	0

xc

2.3 Linearized Equation of Motions

As we observe in Equation 1, the equation is not linear due to the coupling of motion parameters, such as qw and qu, trigonometric functions such as $\sin\theta$ and $\cos\theta$, and non-linear forces and moments resulting from the motion parameters, especially aerodynamics. For easier analysis, we can approximate the dynamics as a linear system using a state-space model.

In this research, we utilize Jacobian matrices for linearization. The Jacobian matrix represents the first-order partial derivatives of a vector-valued function. In the context of dynamics, the Jacobian matrix helps in approximating how small changes in the system variables. By evaluating the Jacobian matrix at an operating point, we can derive a linear approximation of the system dynamics that holds locally around that point.

We analyze and transform the dynamic of the aircraft in a several trimmed point across the flight envelope of transition maneuvers into several linear equations of motions in the form of state space. For a linear-time-invariant system (LTI) the state space model can be written in Equation 6.

$$\begin{aligned}\dot{\vec{x}} &= A\vec{x} + B\vec{u} \\ \vec{y} &= C\vec{x}\end{aligned} \tag{6}$$

Equation 7 defines the state variables crucial for fixed-wing, hover, and transition phases of the UAV, encompassing parameters like θ, u, w, and q.

Furthermore, the input vector for both transition and hover flight is composed of three elements: δ_e, T_{rear}, and T_{front}. For the Meanwhile, the value of δ_{tilt} is directly set depending on the state the aircraft is in. For example, if the aircraft is in hover, the value of δ_{tilt} will automatically be set to 90°. During fixed-wing flight, the parameter T_{rear} in the state machine will automatically set the value to zero, given that the rear motor is deactivated in this mode of operation.

$$\vec{x} = \begin{bmatrix}\theta \\ u \\ w \\ q\end{bmatrix}, \quad \vec{u}\begin{bmatrix}\delta_e \\ T_{rear} \\ T_{front} \\ \delta_{tilt}\end{bmatrix}, \quad \vec{y} = \begin{bmatrix}u \\ w\end{bmatrix} \tag{7}$$

The state matrices, represented by $\mathbf{A}$ and B, vary across different trimmed conditions as defined earlier. In Equation 8, 9, and 10, we provide examples of these matrices for three distinct conditions: fixed-wing flight at a velocity of 18 m/s denoted by fw_{18}, transition with δ_{tilt} set to 60° denoted by $trans_{60}$, and hovering indicated by hov.

$$A_{fw_{18}} = \begin{bmatrix}0.00 & 0.00 & 0.00 & 1.00 \\ -9.81 & -0.033 & 0.411 & -0.437 \\ 0.285 & -0.686 & -6.50 & 22.0 \\ 0.00 & -0.0034 & 0.172 & 0.00\end{bmatrix}, \quad B_{fw_{18}} = \begin{bmatrix}0 & 0 & 0 \\ 0.192 & 0 & 0.222 \\ -11.8 & -0.222 & 0 \\ -39.6 & -0.671 & 0\end{bmatrix} \tag{8}$$

$$A_{trans_{60}} = \begin{bmatrix}0 & 0 & 0 & 1.00 \\ -9.81 & -0.0248 & 0.0950 & 0 \\ 0 & -0.267 & -2.33 & 4.000 \\ 0 & -0.412 & -0.00730 & 0\end{bmatrix}, \quad B_{trans_{60}} = \begin{bmatrix}0 & 0 & 0 \\ -0.117 & 0 & 0.111 \\ -0.596 & -0.222 & -0.193 \\ -1.995 & -0.671 & 0.155\end{bmatrix} \tag{9}$$

$$A_{hov} = \begin{bmatrix}0 & 0 & 0 & 1.000 \\ -9.81 & -0.7979 & 0.0000 & 1.001 \\ 0 & 0.1928 & -0.0001 & 0 \\ 0 & 0.1109 & -0.0001 & 0\end{bmatrix}, \quad B_{hov} = \begin{bmatrix}0 & 0 & 0 \\ 0 & 0 & 0 \\ 0 & -0.2222 & -0.2222 \\ 0 & -0.6711 & 0.1785\end{bmatrix} \tag{10}$$

Meanwhile, the matrix $\mathbf{C}$ remains unchanged across all trim points, as depicted in (11).

$$C = \begin{bmatrix}0 & 1 & 0 & 0 \\ 0 & 0 & 1 & 0\end{bmatrix} \tag{11}$$

2.4 Controllability and Stability of The System

Next, we will proceed with a controllability analysis to evaluate the system's capability to be controlled. This analysis is fundamental in understanding the system's behavior and its responsiveness to control inputs. Controllability is a critical aspect that determines whether the system can be effectively controlled from any initial state to any desired state within a finite time span.

To perform this analysis, we utilize the controllability matrix, denoted as Q in Equation 12. The controllability matrix is derived from the system's dynamics and input matrices. Specifically, it is formulated as follows:

$$Q = \begin{bmatrix} B & AB & A^2B & \cdots & A^{n-1}B \end{bmatrix} \tag{12}$$

Here, A represents the system matrix, B denotes the input matrix, and n represents the number of control inputs. By analyzing the rank of the controllability matrix, we ascertain whether the system is controllable. If the rank of Q equals the system matrix's dimension, then the system is controllable; otherwise, it is not.

Upon conducting the controllability analysis across all trim points, we observed that the tilt-rotor system demonstrates consistent controllability. This implies that regardless of the operating conditions represented by different trim points, the system remains controllable, ensuring that it can be effectively controlled using appropriate control inputs.

In addition to controllability analysis, understanding system stability is crucial. This can be visualized using a pole-zero diagram, which illustrates the location of poles (eigenvalues) and zeros (roots of the transfer function) in the complex plane. Stable systems have poles located in the left half-plane, indicating that they decay over time and are bounded. Unstable systems have poles in the right half-plane, leading to unbounded responses. By analyzing the pole-zero diagram, we can assess the stability of the system under different operating conditions.

We took an example of three trim points: fixed-wing flight with a velocity of 22 m/s, transition with a tilt angle δ_{tilt}, and hover condition, and displayed them in Figure 3. In Figure 3, all of the plants have at least one pole in the positive real axis value, indicating instability. Hence, all of the systems are unstable. The characteristics of other trim points outside of the example are similar, with at least one pole in the positive real axis value, which indicates the instability of the plant. Therefore, a control system is needed to stabilize the UAV at each trim point.

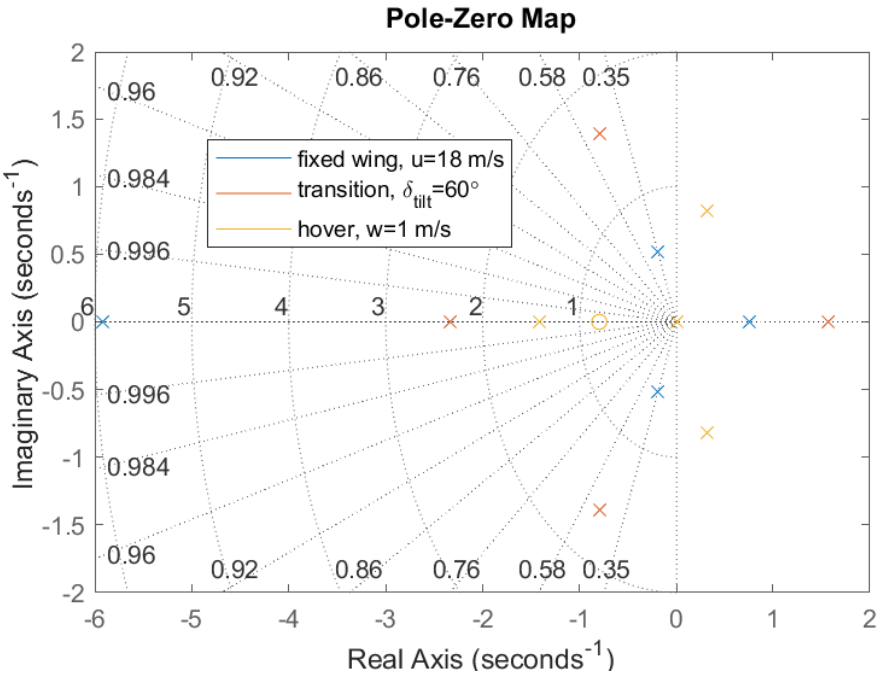

Figure 3 – Pole zero map of RayBe tilt-rotor UAV linearized equation of motion

3. Flight Controller Strategies

Utilizing the linearized equation of motion, we can design an LQG controller tailored for managing the transition dynamics of the tilt-rotor UAV. This entails employing the closed-loop pseudo-block diagram depicted in Figure 4. The controller architecture comprises two loops. The outer loop integrates integral action, which involves incorporating feedback by integrating the error signal within the controller. This integration process facilitates the generation of a feedback term, effectively minimizing steady-state error. Meanwhile, the inner loop employs the state feedback matrix derived from the LQ controller technique, ensuring optimal control over the system's internal dynamics. This controller operates by accepting a reference value $\vec{y}_{ref}$ for both u and w. The discrepancy between this reference and the current output $\vec{y}$ forms the feedback error, which, upon multiplication by the outer gain K_{outer}, yields the refercence state $\vec{x}_{ref}$. Subsequently, the error feedback arising from the Kalman filter state observer model $\hat{x}$ and x_{ref} is processed through the inner gain K_{inner}. This step yields the desired inputs for the dynamic model—namely, δ_e, T_{front}, and T_{aft}. Meanwhile, the determination of the motor tilting angle δ_{tilt} is dictated by the current state of the state machine. For instance, when the aircraft is in the fixed-wing state, δ_{tilt} remains at $0°$, whereas during hover, it equals $90°$. The values of K_{outer} and K_{inner} are dynamically adjusted by the state machine, ensuring optimal controller performance across varying operational states. It's worth noting that these gains are obtained through the LQ controller process, involving the Riccati equation, which will be elaborated upon in the subsequent LQG subsection. The role of the state machine solely lies in switching between these pre-computed gains based on the current operational state.

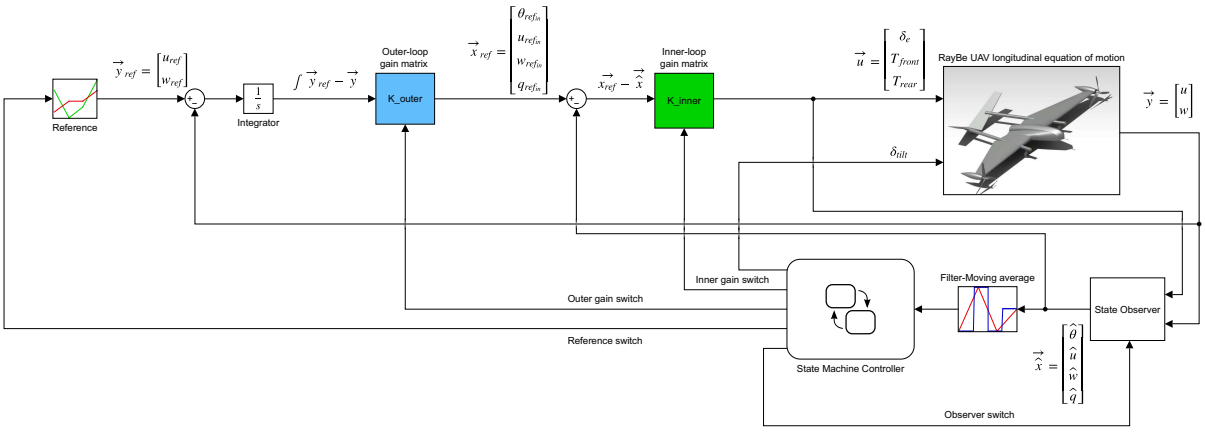

Figure 4 – Control system block diagram

3.1 Linear-Quadratic-Gaussian Controller

The linear-quadratic-Gaussian (LQG) controller, shown in Figure 5, combines two key parts: a Linear Quadratic (LQ) (LQ) controller and a Kalman Filter. It's designed to manage linear stochastic systems that can be affected by process noise in the system dynamics and measurement noise.

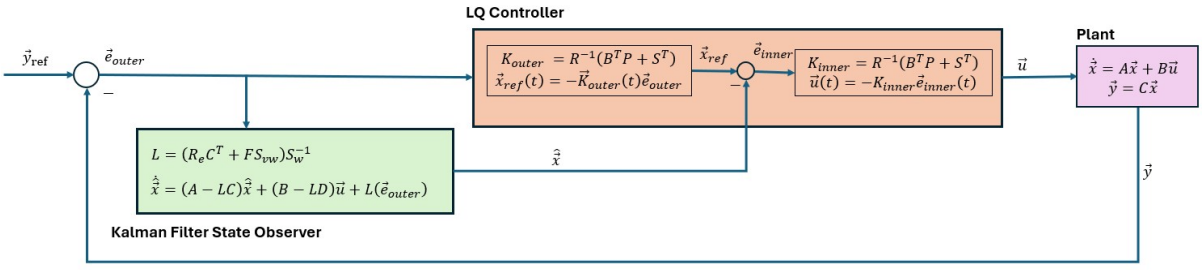

Figure 5 – An LQG compensator for tracking a reference output [12]

The LQG controller helps keep the system stable and performing well, even when there are uncertainties or disturbances. It works by using the Kalman Filter to estimate the current state $\hat{x}$ of the system from noisy measurements. This estimated state provides a more accurate representation of the system's actual state than the raw measurements alone. The Kalman Filter continuously updates the state estimate as new measurements come in, while the LQ controller continuously adjusts the control inputs based on the latest state estimate.
Once the current state is estimated, the LQ controller uses this information to calculate the optimal control input $u(t)$. The LQ controller determines the best control action that minimizes a cost function, which typically includes terms for the system's performance and the effort required to control the system. The optimal control input is given by $u(t) = -K\hat{x}(t)$, where K is the optimal gain matrix. The goal is to achieve the desired system behavior while balancing performance and control effort.

3.1.1 Linear-Quadratic Controller

A linear-quadratic controller aims to minimize a quadratic cost function that penalizes both the deviation of the system's state from a desired trajectory and the control effort required to achieve this trajectory.
Let the desired state be defined as $\vec{x}_{ref}$, then the error vector can be denoted as $\vec{e} = \vec{x}_{ref} - \vec{x}$. In the controller design process, the optimal control is designed to obtain $\vec{u}(t)$ such that the cost function in Equation 13 can be minimized.

$$J = \int_0^\infty \left(\vec{e}^T Q\vec{e} + \vec{u}^T R\vec{u}\right) dt \tag{13}$$

where Q is a positive semi-definite matrix penalizing the state deviation, and R is a positive definite matrix penalizing the control effort.
The control signal u that will minimize J in Equation 13 is given in Equation 14.

$$\vec{u}(t) = -K\vec{e}(t) \tag{14}$$

K is the feedback gain matrix given by Equation 15.

$$K = R^{-1}B^T P \tag{15}$$

where P is the solution of the algebraic Riccati equation in form of positive definite matrix. The algebraic Riccati equation for continuous-time systems is given by Equation 16.

$$A^T P + PA - PBR^{-1}B^T P + Q = 0 \tag{16}$$

Substituting this control law into the dynamics equation, we get Equation 17.

$$\dot{x}(t) = (A - BK)\vec{e}(t) \tag{17}$$

The solution to the Riccati equation provides the optimal feedback gain matrix K, which minimizes the cost function J for the given system dynamics A and control matrices B, as well as the weighting matrices Q and R. Applying this optimal feedback control law results in a closed-loop system that drives the state of the linear system towards the desired trajectory or the trim values while minimizing the cost function over an infinite time horizon.

3.1.2 Kalman Filter

The uncertainties in the tilt-rotor model arise due to the model having only limited linearization points, despite the dynamics in the transition process being highly complex and nonlinear. To address this issue, we propose the idea of using a Kalman Filter state estimator within the LQG controller to provide the best estimation of the system state despite the nonlinear dynamics of the transition process. The Kalman filter is a recursive estimator that combines measurements from sensors with a dynamic model of the system to provide the best estimate of the system's state, taking into account both the inherent uncertainties in the system dynamics and the measurement noise. The Kalman filter works by minimizing the covariance matrix of the estimation error, which can be written in Equation 18:

$$\hat{e}(t) = \vec{x}(t) - \hat{x}(t) \tag{18}$$

where $\hat{x}(t)$ is the estimated state vector and x is the state of the system, whose dynamics are described in Equation 19:

$$\dot{\hat{\vec{x}}}(t) = A_0(t)\hat{\vec{x}}(t) + B_0(t)\vec{u}(t) + L(t)\vec{y}(t) \tag{19}$$

The matrices $A_0(t)$ and $B_0(t)$ are the coefficient matrices of the Kalman Filter, while $u(t)$ represents the input to the system. Additionally, $L(t)$ denotes the Kalman gain applied to the measurement $y(t)$. The equation for the optimal Kalman filter gain is written in Equation 20:

$$L = (R_e C^T + F S_{vw}) S_w^{-1} \tag{20}$$

where S_w is the correlation matrix of the process noise, S_{vw} is the cross-spectral density matrix of process noise and measurement noise, and R_e is the conditional covariance matrix defined as the covariance matrix based on the finite record of the output, which is shown in Equation 21.

$$R_e(t,t) = E[\hat{e}(t)\hat{e}^T(t) | \hat{y}(\tau), t_0 \leq \tau \leq t] \tag{21}$$

In our controller model, the Kalman Filter is specifically designed as a linear parameter-varying model. With this method, we can approximate nonlinear systems and apply linear design techniques to nonlinear models without using more advanced Kalman Filter models, such as the Extended Kalman Filter. The state machine will act as a trigger for parameter changes in the Kalman Filter based on the state of the tilt-rotor UAV.

3.2 State Machine

For the implementation of switching strategies, we employ a state machine as the decision logic mechanism for transitioning between different operational states. This state machine, often referred to as a finite state machine (FSM), operates on a finite set of states, each representing a distinct operational condition. In general, a finite state machine is a mathematical model where there is only exactly one of a set of finite states at a time. By utilizing the finite state machine, the algorithm can be visualized in a way that makes the transition rules between states more interpretable. Finite machines have found applications in different engineering fields, such as UAV energy management strategy [13] and motion controllers for servo drives [14].

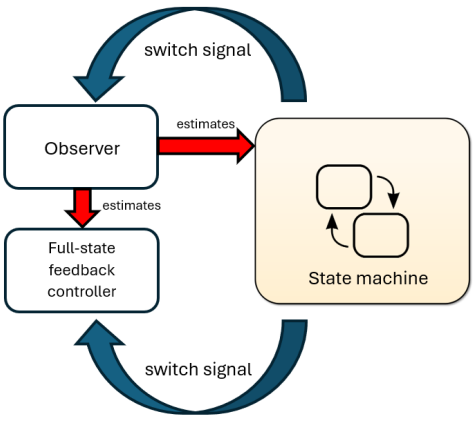

Figure 6 – State machine and controller workflow

In this case, the FSM is constructed, enabling a visual representation of the decision-making process. The state flow model encapsulates the various states, the transitions between them, and the conditions dictating these transitions. Figure 6 shows the interaction between the state machine and the controller. The state machine provides a switch signal for both the observer and the full-state feedback controller. For the observer, the switch signal changes the parameters of the Kalman Filter.

For the feedback controller, the switch signal alters the optimal gain matrix of the LQ controller. The state machine retrieves information about the current state from the system.

4. Nonlinear Simulation

4.1 Simulation Scenario and Setting

In this section, the designed controller will be implemented in the constructed nonlinear simulation. The closed-loop system, as illustrated in Figure 4, is constructed to test the performance of the designed control strategies in longitudinal mode.

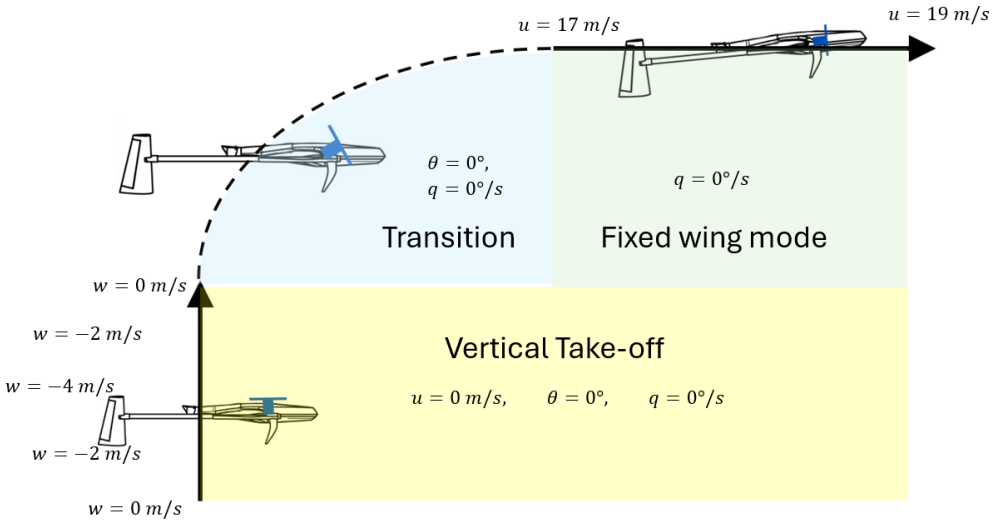

Figure 7 – Simulation mission profile

In the test, as illustrated in Figure 7, the tilt-rotor UAV will start from hover with zero velocity and take off vertically with a speed of 4 m/s. Then, the rotor will be slowly tilted until it is facing forward ($\delta_{tilt} = 0°$), and then continue to perform fixed-wing forward flight (steady symmetrical level flight) from a forward velocity of 17 m/s to 19 m/s. During the vertical take-off maneuver, the state machine sets a tracking reference of zero for forward speed. Meanwhile, for the vertical speed (w), it accelerates from 0 to -2 and then to -4 (upward), before reversing back to -2 and 0 before the transition phase begins. In this vertical take-off phase, the controller compensates the pitch angle to maintain its zero value, ensuring the vehicle moves upward perpendicular to the ground.

During the transition phase, the rotor tilts from 90° to 0° to enable fixed-wing mode flight. Due to this tilting operation, the thrust vector from the front rotor is deflected, resulting in acceleration/deceleration in both the forward and downward directions. Consequently, the state machine disables the outer loop of the dynamic system (setting K_{outer} to a zero matrix), allowing the control system to focus on maintaining the pitch angle (θ) and pitch rate (q). The outer loop is re-enabled when the tilting angle reaches 0°, indicating the vehicle has entered fixed-wing mode. In this mode, the state machine disables the rear rotor, allowing the pitching moment control to solely rely on the elevator.

Figure 8 illustrates the activated set of gain matrices from LQ controller (**K**) based on the current states u and w. To address the nonlinearity of the system, the optimal controller switches based on the control logic contained in the state machine. The colored bounding boxes in the plot depict the regions where each **K** is active.

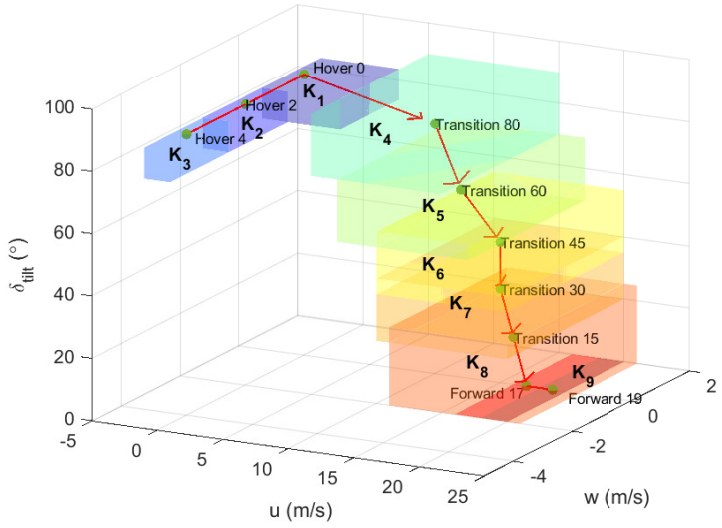

Figure 8 – Gain switching region

4.2 Simulation Result

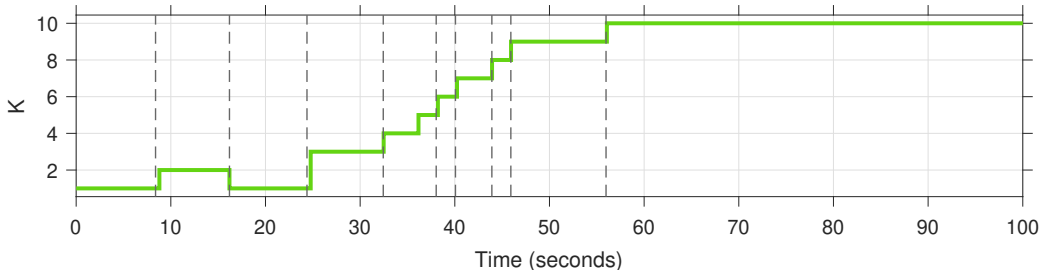

Figure 9 – Gain switching simulation result

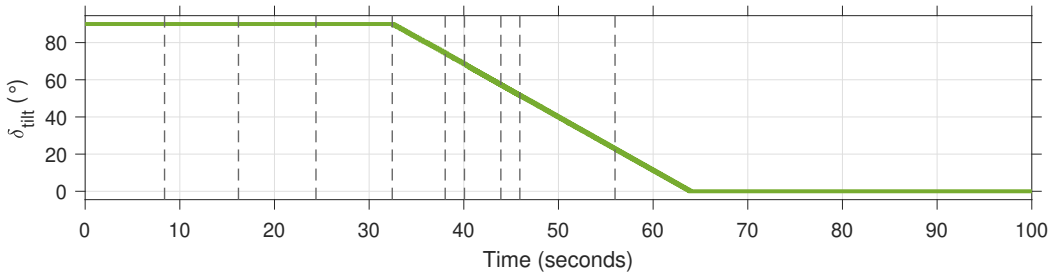

Figure 10 – Tilting angle simulation result

During the simulation, the state machine sequentially performs gain-switching, transitioning from the gains utilized for hover mode, through the transition phase, and ultimately to the fixed-wing flight mode, as shown in Figure 9. As the gains switch, the main rotor gradually tilts forward until it is oriented for fixed-wing flight ($\delta_{tilt} = 0°$) which is depicted in Figure 10. For the initial 32 seconds, the aircraft employs the gains designated for hover mode, specifically $\mathbf{K_1}$ through $\mathbf{K_3}$, with the main rotor oriented upward ($\delta_{tilt} = 90°$). Subsequently, as the aircraft enters the transition process, the state machine adjusts the gain to $\mathbf{K_4}$, and δ_{tilt} starts to change gradually. Throughout the transition process, the state machine continually modifies the applied gains based on the parameters u and w. Upon completion of the transition, the UAV shifts to fixed-wing flight, at which point the state machine adjusts the gain to $\mathbf{K_9}$ with the rotor oriented horizontally ($\delta_{tilt} = 0°$).
The simulation results of the constructed closed-loop system can be seen in Figure 11. From the

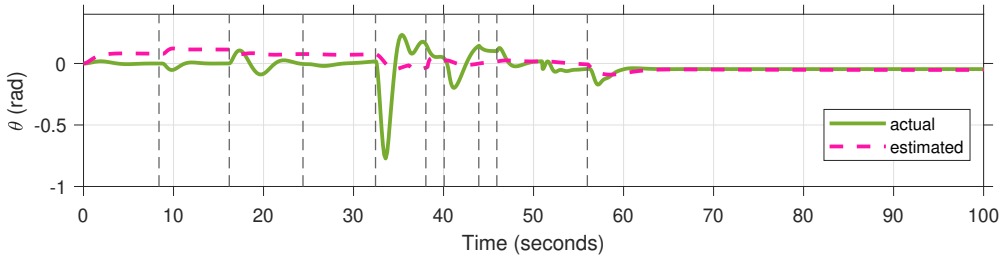

(a) Pitch angle simulation result

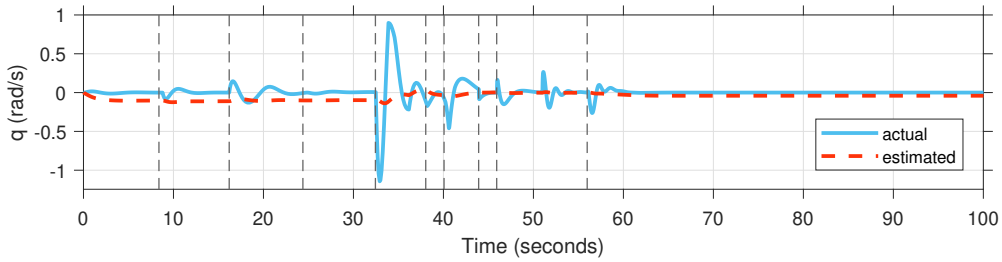

(b) Pitch rate simulation result

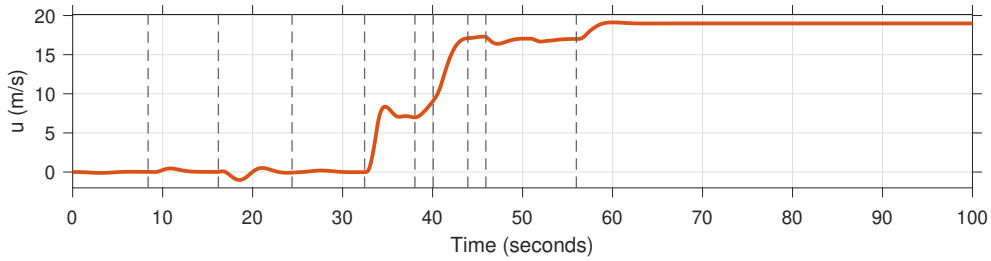

(c) Body axis forward speed simulation result

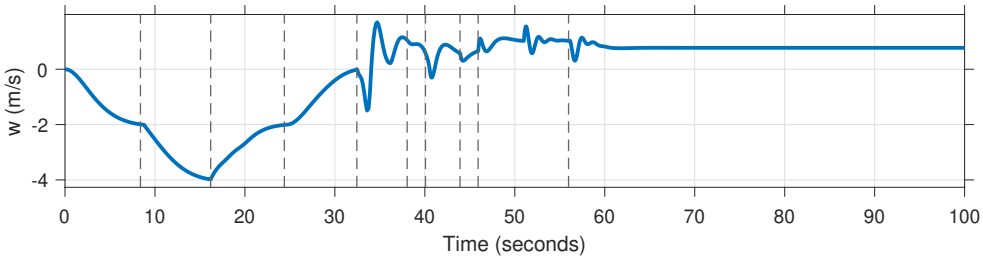

(d) Body axis downward speed simulation result

Figure 11 – Nonlinear simulation state results

simulation results, it can be observed that the designed flight controller strategy can autonomously perform flight from hover (vertical takeoff function) to forward flight (fixed-wing mode). However, there are notable differences between the actual and estimated results for the pitch angle and pitch rate plots. This discrepancy may be attributed to the Kalman Filter's inability to accurately estimate high-frequency signals. While the designed Kalman Filter coupled with the state machine provides sufficient information for the full state feedback controller to maintain stable autonomous operation, the error between the actual and estimated signals persists, especially in the transient region, mostly during the transition phase.

During the operation, Figure 11 shows successful tracking capabilities during the vertical take-off phase. Throughout this phase, the combination of gain matrix scheduling, controlled by the state machine, maintains the body axis forward velocity, u, at zero while increasing the upward velocity $(-w)$. The vehicle achieves a vertical velocity of 2 m/s in 8.4 seconds from 0 m/s, then reaches 4 m/s in the next 7.8 seconds with steady-state errors of 0.375% and 0.425%, respectively. Subsequently, the vehicle decelerates to 0 m/s in 16.02 seconds from an upward velocity of 4 m/s. During the vertical

take-off operation, the vehicle experiences a maximum forward speed of -1 m/s, with a total horizontal displacement of 0.45 m. This test result demonstrates that despite experiencing additional drag and pitch moments while retaining additional upward velocity, the designed flight controller maintains its robustness.

The transition phase lasted 32 seconds, resulting in a displacement of 289.3 m horizontally and 50.8 m vertically. During this phase, the vehicle experienced the most severe pitch angle and pitch rate, reaching a maximum pitching angle of -0.77 rad and a maximum pitch rate of -1.14 rad/s. In this phase, the vehicle regained speed to surpass the stall speed, enabling it to transition into fixed-wing mode flight. By the end of the phase, the vehicle had regained a forward speed of 17 m/s. Analyzing the fixed-wing mode phase, the controller effectively stabilized the system using the pitching moment provided solely by the elevator, indicating that the regained speed was adequate. The controller able to maintain the pitch angle θ and pitch rate q to zero demonstrating a good fixed wing flight quality. Additionally, during fixed-wing mode, the system successfully tracked its velocity to 19 m/s from 17 m/s in 3.3 seconds, with an error of 0.105%.

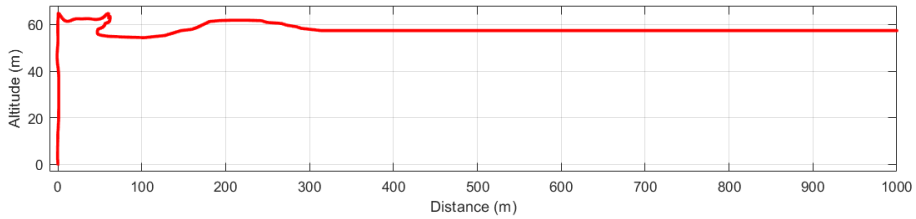

Figure 12 – Trajectory simulation result

The simulation assumes that the tilting UAV starts the vertical take-off phase from the ground (equivalent to 0 altitude). After reaching a certain vertical speed, the UAV transitions to hover mode to begin the transition phase. Based on the trajectory shown in Figure 12, the flight path indicates that with the designed controller method, the UAV can maintain stability during the transition phase without significant loss of altitude.

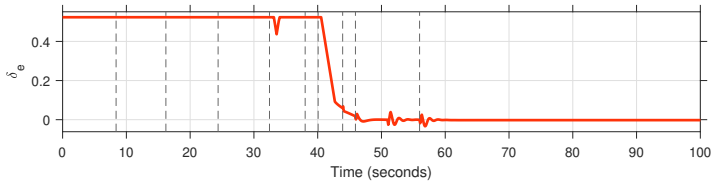

(a) Elevator angle input

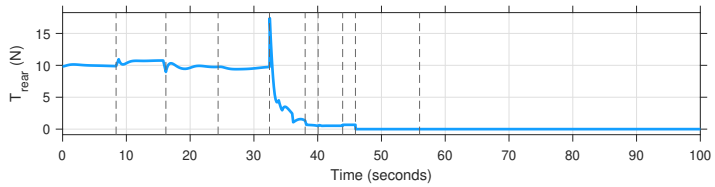

(b) Rear rotor thrust input

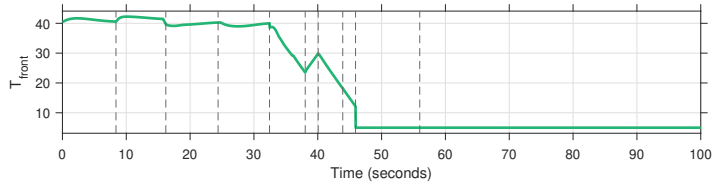

(c) Main rotor thrust input

Figure 13 – Nonlinear simulation input signal

Furthermore, Figure 13 reveals the input signal provided by the control system to the plant during the simulation. Although the system can be controlled with elevator inputs below the maximum deflection angle (in this case $\pm 30^{\circ}$) and the thrust given is still below the maximum thrust (8 kg for each rotor), there is a noticeable rapid change in the rear thrust input. It can be observed from the figure that there is a rapid change in rear thrust during the transition phase due to the necessity of providing additional pitching moments when the thrust vector deflects.

5. Conclusion

The research has demonstrated a new approach to controlling a tilt-rotor UAV, a highly nonlinear system, using an LQG controller coupled with a state machine. With this proposed control method, the capabilities of LQG, which typically only work in specific conditions, can be extended to cover a wider operation regime, involving significant system's dynamics changes. Based on the case study, the tilt-rotor UAV, together with the flight control strategy, can perform autonomous flight from hover condition to forward flight in fixed-wing mode. The test results show that the system can execute a vertical take-off maneuver, reaching 4 m/s upward velocity from 0 m/s in 16.02 seconds. The vehicle can also maintain zero forward velocity during vertical take-off, resulting in an insignificant horizontal displacement of 0.45 m. Additionally, with the proposed control method, the controller can handle the UAV during the transition phase, which is highly nonlinear, by maintaining the pitch attitude of the vehicle. From the simulation, the maximum pitch angle and pitch rate account for -0.77 rad and -1.14 rad/s, respectively, occurring during the transition phase. Moreover, the designed control system can track forward velocity from 17 m/s to 19 m/s during steady symmetrical level flight in fixed-wing mode. However, although the designed observer provides enough information to the full-state feedback controller to stabilize and track, it is notable that the designed Kalman Filter coupled with the state machine still produces significant errors, especially in high-frequency region. For future work, further analysis and validation of the control strategy can be performed using Software-in-the-Loop (SIL) and Hardware-in-the-Loop (HIL) simulations before real-world UAV testing.

6. Contact Author Email Adress

For additional information regarding the paper, feel free to contact the authors using the following email address: joshualevinkurniawan@gmail.com.

7. Copyright Statement

References

[1] A. Misra, S. Jayachandran, S. Kenche, A. Katoch, A. Suresh, E. Gundabattini, S. Selvaraj, and A. Legesse. A review on vertical take-off and landing (vtol) tilt-rotor and tilt wing unmanned aerial vehicles (uavs). Journal of Engineering, Vol. 2022, pp. 1-20, 2022.

[2] Y. Nakamura, A. Arakawa, K. Watanabe, and I. Nagai. Transitional flight simulations for a tilted quadrotor with a fixed-wing. Proc. 2018 IEEE International Conference on Mechatronics and Automation (ICMA), Changchun, China, Vol. 1, pp. 1829–1836, 2018.

[3] D. Yangping and H. Gao. Transition flight control and test of a new kind tilt prop box-wing vtol uav. Proc. 2018 9th International Conference on Mechanical and Aerospace Engineering (ICMAE), Budapest, Hungary, Vol. 1, pp. 90–94, 2018.

[4] C.-C. Peng, T.-S. Hwang, S.-W. Chen, C.-Y. Chang, Y.-C. Lin, Y.-T. Wu, Y.-J. Lin, and W.-R. Lai. Zpetc path-tracking gain-scheduling design and real-time multi-task flight simulation for the automatic transition of tilt-rotor aircraft. Proc. 2010 IEEE Conference on Robotics, Automation and Mechatronics, Singapore, Vol. 1, pp. 118–123, 2010.

[5] M. Allenspach and G. J. J. Ducard. Nonlinear model predictive control and guidance for a propeller-tilting hybrid unmanned air vehicle. Automatica, Vol. 132, No. 109790, pp. 1-15, 2021.

[6] D. Liao-McPherson, M. M. Nicotra, and I. Kolmanovsky. Time-distributed optimization for real-time model predictive control: Stability, robustness, and constraint satisfaction. Automatica, Vol. 117, No. 108973, pp. 1-10, 2020.

[7] O. R. González and A. G. Kelkar. Robust multivariable control. In The Electrical Engineering Handbook, Elsevier, pp. 1037-1050, 2004.

[8] J. Roskam. Airplane flight dynamics and automatic flight controls. DARcorporation, 1st edition, 1998.

[9] M. Drela. XFLR5 v6.02 Guidelines, Analysis of foils and wings operating at low Reynolds numbers. Version 6.02, pp. 1-50, February 1986.

[10] McDonnell Douglas Astronautics Company. The USAF Stability and Control DATCOM. St. Louis Division, St Louis, Missouri, Updated by Public Domain Aeronautical Software, pp. 1-500, December 1999.

[11] R. W. Beard and T. W. McLain. Small Unmanned Aircraft: Theory and Practice. Princeton University Press, 1st edition, 2012.

[12] A. Tewari. Advanced control of aircraft, spacecraft and rockets. John Wiley Sons, 1st edition, 2011.

[13] X. Zhang, L. Liu, and Y. Dai. Fuzzy state machine energy management strategy for hybrid electric uavs with pv/fuel cell/battery power system. International Journal of Aerospace Engineering, Vol. 2018, No. 1, pp. 1-10, 2018.

[14] K. Jezernik, R. Horvat, and J. Harnik. Finite-state machine motion controller: Servo drives. IEEE Industrial Electronics Magazine, Vol. 6, No. 3, pp. 13–23, 2012.